H. Lian[1]
Department of Mechanical Engineering,
University of Michigan,
1231 Beal Avenue,
Ann Arbor, MI 48109
e-mail: hlian@umich.edu

J. B. Martz
Department of Mechanical Engineering,
University of Michigan,
1231 Beal Avenue,
Ann Arbor, MI 48109

B. P. Maldonado
Department of Mechanical Engineering,
University of Michigan,
1231 Beal Avenue,
Ann Arbor, MI 48109

A. G. Stefanopoulou
Department of Mechanical Engineering,
University of Michigan,
1231 Beal Avenue,
Ann Arbor, MI 48109

K. Zaseck
Toyota Motor Engineering and
Manufacturing North America, Inc.,
1555 Woodridge Avenue,
Ann Arbor, MI 48105
e-mail: kevin.zaseck@toyota.com

J. Wilkie
Toyota Motor Engineering and
Manufacturing North America, Inc.,
1555 Woodridge Avenue,
Ann Arbor, MI 48105

O. Nitulescu
Toyota Motor Engineering and
Manufacturing North America, Inc.,
1555 Woodridge Avenue,
Ann Arbor, MI 48105

M. Ehara
Toyota Motor Engineering and
Manufacturing North America, Inc.,
1555 Woodridge Avenue,
Ann Arbor, MI 48105

Prediction of Flame Burning Velocity at Early Flame Development Time With High Exhaust Gas Recirculation and Spark Advance

Diluting spark-ignited (SI) stoichiometric combustion engines with excess residual gas improves thermal efficiency and allows the spark to be advanced toward maximum brake torque (MBT) timing. However, flame propagation rates decrease and misfires can occur at high exhaust gas recirculation (EGR) conditions and advanced spark, limiting the maximum level of charge dilution and its benefits. The misfire limits are often determined for a specific engine from extensive experiments covering a large range of speed, torque, and actuator settings. To extend the benefits of dilute combustion while at the misfire limit, it is essential to define a parameterizable, physics-based model capable of predicting the misfire limits, with cycle to cycle varied flame burning velocity as operating conditions change based on the driver demand. A cycle-averaged model is the first step in this process. The current work describes a model of cycle-averaged laminar flame burning velocity within the early flame development period of 0–3% mass fraction burned. A flame curvature correction method is used to account for both the effect of flame stretch and ignition characteristics, in a variable volume engine system. Comparison of the predicted and the measured flame velocity was performed using a spark plug with fiber optical access. The comparison at a small set of spark and EGR settings at fixed load and speed, shows an agreement within 30% of uncertainty, while 20% uncertainty equals ± one standard deviation over 2000 cycles. [DOI: 10.1115/1.4035849]

1 Introduction

Diluting spark-ignited (SI) stoichiometric combustion engines with excess residual gas reduces throttling losses and improves thermal efficiency [1]. In normal operation, the spark is advanced toward maximum break torque (MBT) timing. However, combustion instability, misfire, and knock limit the feasible range of spark timings. For certain operating conditions, it is desirable to continuously operate at the border of the feasible spark region. For instance, with high EGR dilution, the MBT timings are located at a spark advance beyond the misfire limit [2].

Traditionally, spark timing is an open-loop feedforward control with misfire limits determined for a specific engine from extensive experiments covering a large range of speed, torque, and actuator settings, for example, following the approach of Quader [3]. To extend the benefits of dilute combustion while at the misfire limit, it is essential to define a parameterizable, physics-based model capable of predicting the misfire limit as operating conditions change based on driver demand. A predictive model could greatly accelerate the control of highly dilute SI combustion.

In order to model misfire limits with misfires occurring at a given small but arbitrary percentage of the cycle, i.e., 0.8%, it is essential to model flame burning velocity from cycle-to-cycle. The cycle-averaged flame burning velocity at the misfire limits is

the first step toward predicting these limits, with cyclic variation further introduced by cyclic dispersed model parameters describing the governing mechanisms of misfire. Thus, the goal of the current work is to develop a physics-based model of the cycle-averaged flame burning velocity at misfire limits of dilute stoichiometric combustion that can be later extended for predicting both misfire and combustion cyclic variability.

The current work describes a model of laminar flame burning velocity during the early flame development period of 0–3% of mass fraction burned, when the flame radius is smaller than 5 mm with negligible pressure rise from combustion. This early phase accounts for roughly 30–40% of the total combustion duration and is considered to be critical in determining misfire occurrence and overall combustion quality [4]. The model consists of two main components: a kernel initiation model [5] and a correlation-based laminar flame speed model [6]. The kernel initiation model, based on thermal diffusion flame ball theory, predicts if the flame kernel is successfully initiated and also corrects the unstretched and adiabatic laminar flame speed to account for the effects of flame stretch, ignition energy, and heat loss.

The paper is organized as follows: Section 2 presents each of the submodels, while Sec. 3 details the measurement of flame burning velocity with an AVL VisioFlame fiber optic spark plug. Section 4 compares modeled flame burning velocity predictions with measured cycle-averaged flame burning velocities at conditions with varying spark timing and EGR rate. Finally, the paper concludes with discussions of the model extensions for predicting the combustion cyclic variability at the misfiring limit.

2 Model Description

The model consists of two main components outlined in Fig. 1: A kernel initiation model [5] developed from thermal diffusion flame ball theory and a correlation-based laminar flame speed model [6]; both models are executed on a crank angle base. The nondimensional flame kernel model returns a spherical flame trajectory, represented by the normalized flame burning velocity $\widetilde{U}$ and the normalized flame radius $\widetilde{R}$. This constant volume static model has been adapted in a variable volume system to provide correction to the unstretched and adiabatic laminar flame burning velocity prediction $S_{L,u}^0$ and $S_{L,b}^0$ to account for the effects of curvature-induced flame stretch. The flame kernel model depends solely on the normalized ignition power $\widetilde{P}_s$. The laminar flame speed model returns laminar flame burning velocity $S_{L,u}^0(\theta)$ and $S_{L,b}^0\theta$ with respect to the unburned and burned gases, as well as the laminar flame thickness $\delta^0(\theta)(\theta)$, flame reaction front time scalce $t_f^0(\theta)$. Inputs to this model are described in Secs. 2.1 to 2.3.

2.1 Flame Kernel Model. This section briefly describes a nondimensional flame kernel model theoretically studied by Chen

and Ju [5] with the concept of flame ball proposed by Ronney and Sivashinsky [7]. A detailed description of this model can be found in Ref. [5]. An improvement made in the current work is the numerical simplification on the integration term which enables fast computation with online potential. Some supplemental derivations to the work of Chen and Ju are included in the Appendix.

The nondimensional flame kernel model describes the radial flame velocity, along with the curvature-induced stretching and flame kernel failure due to insufficient ignition energy. Neglecting radiation heat loss, the theoretically derived relationship between the nondimensional normalized flame radius $\widetilde{R} = R_f/\delta^0$ and flame burning velocity $\widetilde{U} = S_{L,b}/S_{L,b}^0$ is expressed as

$$\widetilde{T}_f \cdot \frac{\widetilde{R}^{-2} e^{-\widetilde{U}\widetilde{R}}}{\int_{\widetilde{R}}^{\infty} \widetilde{\tau}^{-2} e^{-\widetilde{U}\widetilde{\tau}} d\widetilde{\tau}} - \widetilde{P}_s \widetilde{R}^{-2} e^{-\widetilde{U}\widetilde{R}} \tag{1a}$$

$$= \frac{1}{\text{Le}} \frac{\widetilde{R}^{-2} e^{-\widetilde{U}Le\widetilde{R}}}{\int_{\widetilde{R}}^{\infty} \widetilde{\tau}^{-2} e^{-\widetilde{U}Le\widetilde{\tau}} d\widetilde{\tau}} \tag{1b}$$

$$= \exp\left[\frac{Z}{2} \frac{\widetilde{T}_f - 1}{\widetilde{e}_T + (1 - \widetilde{e}_T)\widetilde{T}_f}\right] \tag{1c}$$

where $\widetilde{\tau}$ is a small radius increment; $\widetilde{e}_T = T_\infty/T_{ad}$ is the expansion ratio; Le, Z are the Lewis number and Zel'dovich number; $\widetilde{T}_f$ is the flame front temperature normalized by the adiabatic flame temperature, where $\widetilde{T}_f = T_f/T_b = 1$. $\widetilde{P}_s$ is the normalized ignition power, defined as

$$\widetilde{P}_s = \frac{P_s}{4\pi\lambda\delta^0(T_b - T_u)} \tag{2}$$

where λ is the thermal conductivity, and δ^0 is the laminar flame thickness obtained from Middleton et al. [6].

Assuming unity Lewis number (Le = 1) and thermal conductivity λ equals 0.1 [$W/m - k$] [8], Eq. (1) is further simplified to

$$\widetilde{R}^{-2} e^{-\widetilde{U}\widetilde{R}} \Big/ \int_{\widetilde{R}}^{\infty} \widetilde{\tau}^{-2} e^{-\widetilde{U}\widetilde{\tau}} d\widetilde{\tau} = 1 + \widetilde{P}_s \cdot \widetilde{R}^{-2} e^{-\widetilde{U}\widetilde{R}} \tag{3}$$

A potential limitation of the current kernel model is its unity Lewis number assumption and the neglect of varying mass and thermal diffusivities, which merit further evaluation in the future work.

An analytical solution does not exist for the integration $\int_{\widetilde{R}}^{\infty} \widetilde{\tau}^{-2} e^{-\widetilde{U}\widetilde{\tau}} d\widetilde{\tau}$ in Eq. (3), so it is solved numerically with the trapezoidal rule for τ in the vicinity of 1. The function $\widetilde{\tau}^{-2} e^{-\widetilde{U}\widetilde{\tau}} d\widetilde{\tau}$
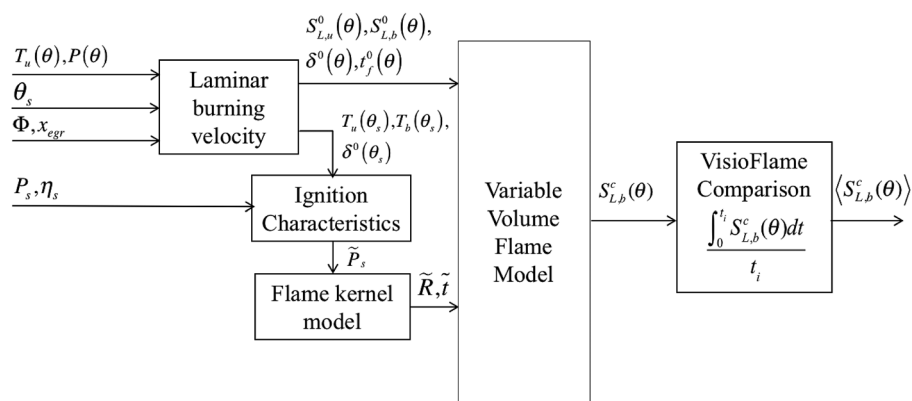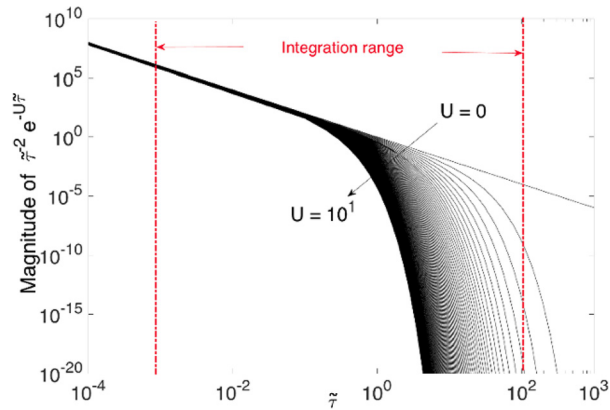

Fig. 1   Model outline

Fig. 2 Numerical integration range of $\widetilde{\tau}^{-2} e^{-\widetilde{U}\widetilde{\tau}} d\widetilde{\tau}$

decreases exponentially with $\widetilde{\tau}$ as shown in Fig. 2. The range of the normalized flame radius $\widetilde{R}$ is bounded to 10^{-3}–10^{2} without sacrificing computational accuracy.

When sweeping the normalized flame radius $\widetilde{R}$ in the range of 10^{-3}–10^{2}, Eq. (3) yields the flame burning velocity for a given normalized flame radius. With sufficient ignition power for a viable flame kernel, the normalized time $\widetilde{t}$ is approximated from normalized flame radius $\widetilde{R}$ and flame burning velocity $\widetilde{U}$

$$\widetilde{U} = \frac{d\widetilde{R}}{d\widetilde{t}} \qquad (4a)$$

$$d\widetilde{t} = \frac{1}{d\widetilde{U}} d\widetilde{R} \qquad (4b)$$

$$\widetilde{t} = \int_0^{\widetilde{R}} 1\widetilde{U} d\widetilde{R} \qquad (4c)$$

An example of the relationship in Eq. (3) is shown in Fig. 3 with varied normalized ignition power illustrating the transition from unsuccessful (discontinued curves) to successful (continued curves) kernel initiation. The normalized flame burning velocity converges to 1 as flame radius increases, suggesting that the effect of geometric flame stretch becomes insignificant at large R, and the flame burning velocity approaches $S_{L,b}^0$. Note that unsuccessful
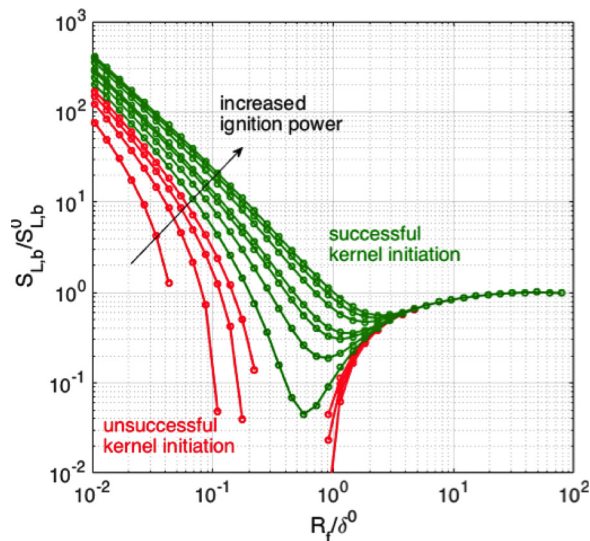

Fig. 3 Relationship between the normalized flame radius $\widetilde{R} = R_f/\delta^0$ and flame burning velocity $\widetilde{U} = S_{L,b}/S_{L,b}^0$ for varying normalized ignition power $\widetilde{P}_s$ based on Eq. (3)

kernels continue at normalized radii of 10^0–10^2. This indicates an unsustainable flame. The solution in this region numerically satisfies Eq. (3), however, the discontinuity indicates that the flame ball can not develop from the energy source, thus interpreted as unsuccessful kernel initiation.

In summary, the relationship between normalized flame radius $\widetilde{R} = R_f/\delta^0$ and the flame burning velocity $\widetilde{U} = S_{L,b}/S_{L,b}^0$ is determined from a single input of the normalized ignition power $\widetilde{P}_s$, models the transition from unsuccessful to successful kernel initiation.

2.2 Laminar Burning Velocity Model. This section documents the laminar burning velocity correlation of Middleton et al. [6], which is based on unstretched isooctane-air laminar flame simulations with varying levels of EGR dilution. The model is used to dimensionalize the relationship between the normalized flame radius $\widetilde{R} = R_f/\delta^0$ and flame burning velocity $\widetilde{U} = S_{L,b}/S_{L,b}^0$ provided by the kernel initiation model.

In the work of Middleton, $S_{L,u}^0$ is the laminar flame burning velocity with respect to the unburned mixture, δ is the laminar flame thickness, and T_b is the adiabatic flame temperature. These variables are correlated from simulations to the unburned temperature T_u in front of the flame, the in-cylinder pressure P, the residual fraction x_r, and the local fuel-to-charge equivalence ratio ϕ' corrected for the dilution of external residual fraction x_{egr}, where Φ is the global equivalence ratio.

In order to compare with the experimental measurement described in Sec. 3, the laminar flame burning velocity $S_{L,b}^0$ with respect to the burned gas [9] is estimated from $S_{L,u}^0$ derived from the work of Middleton. Mass continuity at the flame front yields [9]

$$S_{L,b}^0 = \frac{\rho_u}{\rho_b} S_{L,u}^0 \qquad (5)$$

Invoking the ideal gas law, Eq. (5) is approximated as

$$S_{L,b}^0 = \frac{T_b}{T_u} S_{L,u}^0 \qquad (6)$$

where T_b is the adiabatic flame temperature correlation from Ref. [6], and T_u is the temperature of unburned mixture in front of the flame.

The model is executed at each crank angle during the early flame development period, which corresponds to 0–3% mass fraction burned, when the pressure rise due to combustion is not significant. The polytropic compression pressure and temperature are used in the current modeling work. The process of determining the in-cylinder pressure $P(\theta)$ and temperature $T_u(\theta)$ via polytropic compression is detailed below [10,11].

Neglecting the pressure drop over the valves and intake runner, the intake manifold pressure at intake valve closing (IVC) defines the pressure $P(\theta_{IVC})$ at the beginning of the compression stroke

$$P(\theta_{IVC}) = P_{im}(\theta_{IVC}) \qquad (7)$$

The crank angle for IVC is used as a tuning parameter to compensate the pressure drop and improve the accuracy of estimating the compression pressure P

$$P(\theta) = P(\theta_{IVC}) \times \left(\frac{V(\theta_{ivc})}{V(\theta)}\right)^{\gamma_c} \qquad (8)$$

The compression temperature dynamics are expressed in Eq. (9) as a function of crank angle θ given the initial temperature at IVC $T(\theta_{ivc})$

$$T_u(\theta) = T(\theta_{ivc}) \times \left(\frac{V(\theta_{ivc})}{V(\theta)}\right)^{\gamma_c - 1} \qquad (9)$$

The polytropic exponent γ_c is assumed to be a value of 1.32.

The motoring temperature trace represents the in-cylinder temperature evolution without combustion, and is assumed to be equivalent to the unburned temperature $T_u(\theta)$ in front of the flame during the flame development period.

Assuming the same specific heat for the externally recirculated exhaust gas, internal residual and the fresh air and fuel charge, the temperature at IVC is approximated in Eq. (10) following the approach of Eriksson and Andersson [11]

$$
\begin{aligned}
T(\theta_{\text{ivc}}) = &\, T_{\text{im}}(\theta_{\text{ivc}})(1 - x_{\text{egr}} - x_{\text{ir}}) \\
&+ T_{\text{egr}}(\theta_{\text{ivc}})x_{\text{egr}} + T_{\text{exh}}(\theta_{\text{ivc}})x_{\text{ir}}
\end{aligned}
\tag{10}
$$

where T_{im}, T_{egr}, and T_{exh} are the temperature measurements at the intake manifold, EGR runner, and exhaust runner, respectively. The internal residual fraction x_{ir} and the exhaust gas recirculation fraction x_{egr} are estimated from computational fluid dynamics (CFD). For the current work, the internal residual fraction x_{ir} is assumed to be a constant value of 12% with fixed intake and exhaust valve timings, while the EGR fraction x_{egr} varies with different EGR valve openings.

In summary, given residual fraction x_r and local fuel to charge equivalence ratio ϕ' corrected for dilution under stoichiometric condition, the laminar burning velocity $S_{L,b}^0$ and $S_{L,u}^0$, laminar flame thickness δ^0, and flame reaction front timescale t_f^0 are determined from pressure P and unburned temperature T_u at each crank angle θ during the early phase of combustion after ignition timing θ_s.

2.3 Variable Volume Flame Model and Curvature Correction. For variable volume engine applications, the pressure and temperature evolve as a function of crank angle θ. Limited by the quasi-steady assumption of the flame kernel model, the flame evolution is estimated as discretized events with negligible change in pressure and temperature at a given crank angle. The dimensionalization of the relationship between the normalized flame radius $\widetilde{\mathbf{R}} = \mathbf{R_f}/\delta^0$ and flame burning velocity $\widetilde{\mathbf{U}} = \mathbf{S_{L,b}}/S_{L,b}^0$, is performed on crank angle basis in the variable volume flame model. The crank angle resolve dimensionalization also correct for the flame stretching induced by flame curvature.

At a given crank angle, the flame trajectory of the spherical flame ball with a flame radius $\mathbf{R_f}$ and flame travel time $\mathbf{t}$ is dimensionalized from the normalized flame trajectory ($[\widetilde{\mathbf{R}}, \widetilde{\mathbf{t}}]$), the laminar flame thickness δ^0, and the flame reaction front timescale t_f^0 shown in Eq. (11)

$$
\begin{aligned}
\mathbf{R_f}(\theta) &= \widetilde{\mathbf{R}} \times \delta^0(\theta) \\
\mathbf{t}(\theta) &= \widetilde{\mathbf{t}} \times t_f^0(\theta)
\end{aligned}
\tag{11}
$$

To correct for stretching induced by flame curvature, the corrected laminar flame burning velocity $S_{L,b}^c(\theta)$ is defined as the local derivative. An integral analysis is performed on the crank angle-resolved flame burning velocity correction and are considered to be an approximate of the variable volume process. In this paper, it is calculated using backward Euler method from the flame trajectory at each crank angle with $\Delta\theta = 1$ deg, the numerical uncertainty is of the interest for future work

$$
S_{L,b}^c(\theta) = \frac{R_f(\theta) - R_f(\theta - \Delta\theta)}{t_\theta(\theta) - t_\theta(\theta - \Delta\theta)}
\tag{12}
$$

where t_θ is crank angle resolved given the time to crank angle conversion as

$$
t_\theta(\theta) = (\theta - \theta_s)/(6 \times \text{RPM})
\tag{13}
$$

The process described in Eqs. (11)–(13) is illustrated in Fig. 4. In the upper left corner, the nondimensional trajectory $\widetilde{\mathbf{R}}$ and $\widetilde{\mathbf{t}}$ are computed at the time of spark with over M dimensionless flame radii. The laminar flame thickness δ^0 and flame time scale t_f^0 are updated on crank angle basis until N degrees after the ignition timing θ_s. With which, the nondimensional trajectories $\widetilde{\mathbf{R}}$ and $\widetilde{\mathbf{t}}$ are scaled back to physical dimensions at each crank angle, resulting in M by N matrices of $\mathbf{R_f}$ and $\mathbf{t}$. The corrected laminar flame burning velocity $S_{L,b}^c(\theta)$ is defined from the diagonal components of the matrices of $\mathbf{R_f}$ and $\mathbf{t}$.

The first ten flame trajectories of flame radius $\mathbf{R_f}$ and flame time $\mathbf{t}$ from 1 to 10 deg after ignition timing are plotted in black lines in Fig. 5. The corrected laminar flame burning velocity is defined locally as the slope of red dashed line segments.
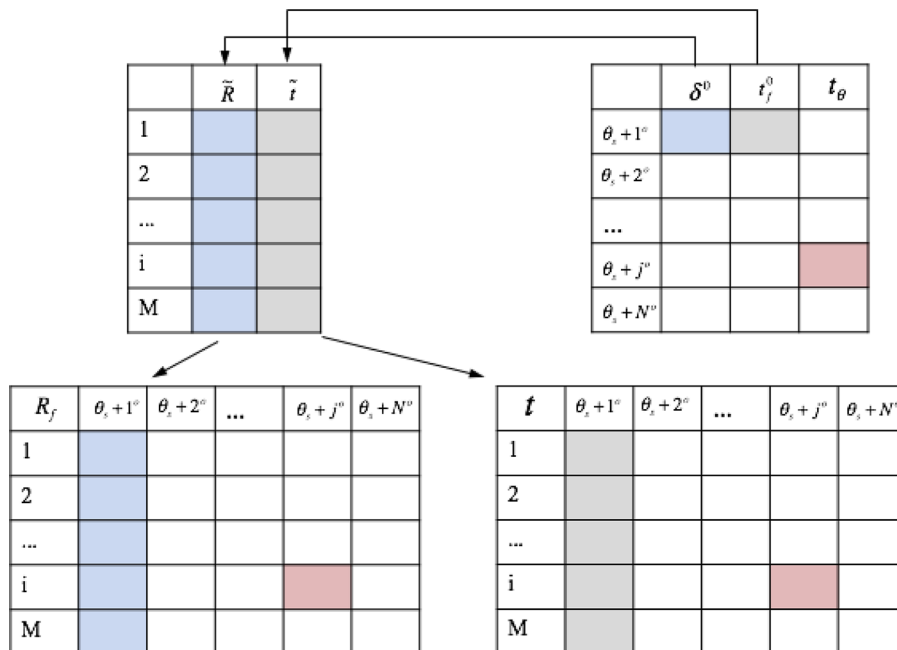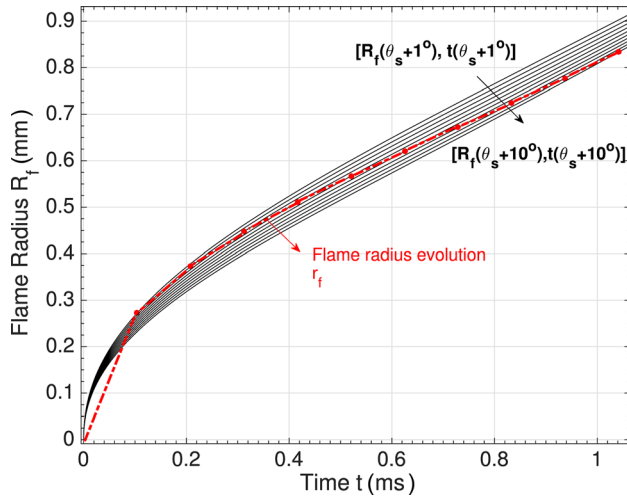

Fig. 4 Dimensionalization process

Fig. 5 The laminar flame burning velocity $S_{L,b}^c(\theta)$ corrected for curvature stretching and ignition deposition from 1 to 10 deg after ignition timing θ_s

The crank angle-resolved laminar flame burning velocity $S_{L,u}^0$, $S_{L,b}^0$ and the corrected laminar flame burning velocity $S_{L,b}^c$ are shown in Fig. 6 at 45 deg bTDC spark timing and 25% EGR rate. $S_{l,u}^0$ is approximately 3–4 times higher than $S_{L,b}^0$ due to the burned gas expansion effect, $S_{L,b}^0$ is further corrected for curvature stretching effect as $S_{L,b}^c$. The correction causes 5–30% deviation on unstretched $S_{L,b}^0$. It should be noted that at the initial phase (<10 deg) after ignition, the corrected flame burning velocity $S_{L,b}^c$ is higher than the laminar burning velocity $S_{L,b}^0$. This is caused by the deposition of ignition energy during the first few hundred microseconds, shown as the steeper slope $dR_{f,k}/dt_k$ in the range of 10^{-1} ms in Fig. 5. The effect of ignition energy decreases with $\widetilde{R}$ as the flame moves away from the ignition energy source.

To estimate the flame radius evolution in a variable volume engine system, the derivations at constant volume should be treated as differential terms and adopt the integral analysis [12]. Discussion on the limitations associated to the adoption of quasi-steady flame kernel model is given in the Appendix. The flame radius evolution r is expressed in Eq. (14) with the flame travel time history t converted from the crank angle evolution (Eq. (13)), with its discretization equivalent to the red line segments shown in Fig. 5
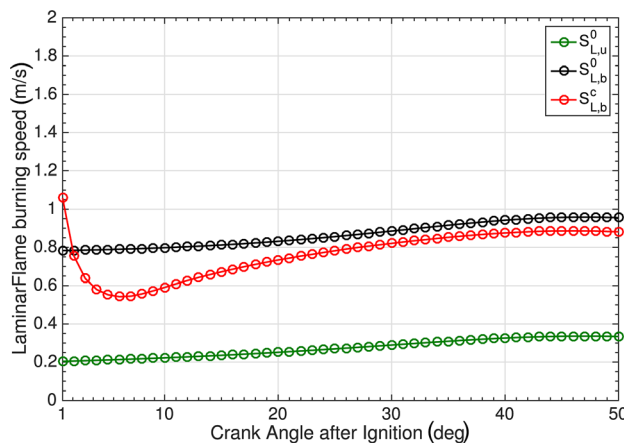

Fig. 6 Crank angle-resolved laminar flame burning velocity $S_{L,u}^0$, $S_{L,b}^0$ with respect to the unburned/burned mixture, and the corrected laminar flame burning velocity $S_{L,b}^c$ (45 deg bTDC spark timing and 25% EGR rate)

Table 1 Engine parameters

Compression ratio	13.5
Displacement (cc)	1329
Stroke (mm)	80.5
Bore (mm)	72.5
Engine speed (RPM)	1600
Engine load (NM)	50
Injection strategy	PFI
Global equivalence ratio	1
Intake charge composition	Air
Intake air volume flow rate (cc/s)	8
Intake charge temperature (K)	370
Number of repetitive cycles	2000

$$r = \int_0^t S_{L,b}^c(t)dt \qquad (14)$$

In order to validate the modeled cycle-averaged flame burning velocity, comparisons are provided with flame velocity measurements from AVL VisioFlame fiber optic spark plug at operating conditions with various EGR rates and spark timings.

3 Experimental Setup

A production 1.3 L four-cylinder Toyota port fuel injection (PFI) SI engine (1NR-FKE) equipped with high pressure loop EGR was used for the experimental validation. The EGR actuator controls the volume fraction of exhaust gas recirculation, where a wide open EGR valve increases EGR fraction until saturation. The EGR actuator is located upstream of the intake runners. The engine is naturally aspirated, port fuel injected, and hence, it is considered well-premixed. The engine parameters are summarized in Table 1. The conventional spark plug is modified and replaced by a VisioFlame fiber optic spark plug which records the flame arrival time. The engine is equipped with in-cylinder pressure sensors with pressure data acquired every 1 crank angle degree (CAD) to obtain pressure at intake valve closing (IVC). The pressure at IVC can also be estimated from manifold pressure.

The experimental conditions reported in this paper are summarized in Table 2 with different spark timings, θ_s and estimated EGR rates.

3.1 VisioFlame Fiber Optic Spark Plug. The AVL VisioFlame fiber optic spark plug was built from a standard spark plug. The cross section of the modified spark plug is illustratively sketched in Fig. 7. There are eight channels of light signals from seven light detection fiber optic probes, each with 5 mm radius from the center of the spark plug. The signal of the eighth channel is extrapolated from the two adjacent probes. The fiber optics are protected from high in-cylinder temperature by sapphire windows welded to the spark plug, which also ensure probe sealing to prevent deposit build up and loss in light transmissions.

The fiber optic records the light intensities emitted as the flame passes the window. The seven photomultiplier signals are calibrated before measurement so that a uniform threshold is applied to all the light signals. The flame arrival time for each probe t_i is defined when the light intensity exceeds the threshold. An

Table 2 Experimental conditions

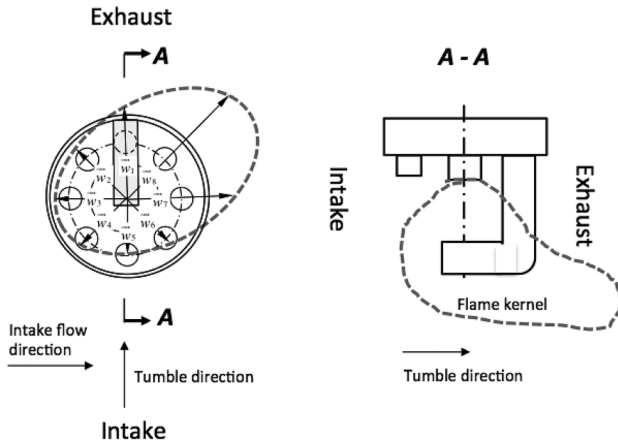| Spark timing (deg bTDC)	14	25	35	40	45
EGR rates					
0%	*				
13%		*			
22%			*	*	*
24%			*	*	
25%			*	*	*

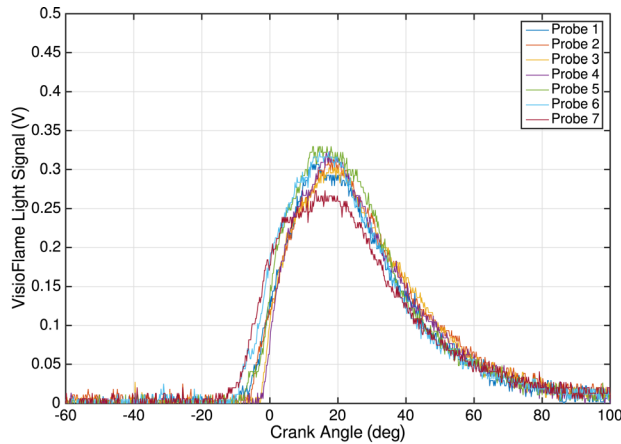**Fig. 7 Illustration of the VisioFlame fiber optic spark plugs**

Fig. 8 An example of the superimposed seven photomultiplier signals (45 deg bTDC spark timing and 25% EGR rate)

example of the seven photomultiplier signals is shown in Fig. 8. The postprocessing principles for the flame speed measurement are discussed below, however, the choice of the threshold and details on the AVL postprocessing algorithm can be found elsewhere [4,13].

A vector of measured flame velocity is defined with its magnitude equaling $w_i = dr_f/dt_i$ and direction determined from the probe orientation. The flame kernel growth rate w describing the flame kernel contour growth rate is defined from $\mathbf{w}_i$ as

$$w = \frac{\sum_1^8 |\mathbf{w}_i|}{8} \tag{15}$$

The flame drift velocity v_f describes the directional movement of the flame center mass. The flame drift velocity v_f is defined as the scalar component of the vector summation of $\mathbf{w}_i$.

3.2 Measurement of Flame Burning Velocity $S_{t,b}$. The difference between the measured flame growth rate and the flame burning velocity has been reviewed and summarized by Andrews and Bradley [14]. Assuming the flow velocity v_g in the unburned region is normal to the flame front, the measured flame growth rate w is approximated as

$$w = \frac{dr_f}{dt} = v_{g,u} + S_{b,u} \tag{16}$$

with $S_{b,u}$ as the flame burning velocity with respect to the unburned mixture.

With mass and kinematic balances at the flame front [9], the relationship of Eq. (16) can also be expressed with respect to the burned gas

$$\frac{dr_f}{dt} = v_{g,b} + S_{t,b} \tag{17}$$

where $v_{g,b}$ is the flow velocity on the burned side behind the flame, for a symmetric spherical flame propagation, the flow velocity $v_{g,b}$ is zero. $S_{t,b}$ is the flame burning velocity with respect to the burned gas.

The flame drift velocity v_f measured from VisioFlame spark plug describes the directional movement of the flame kernel center of mass and is directly linked to the flow motion in the burned side. Thus, the flame drift velocity is representative of the gas velocity behind the flame. In the current paper, we assume

$$v_f = v_{g,b} \tag{18}$$

So that the flame burning velocity $S_{t,b}$ with respect to the burned side is determined from the measurements as

$$S_{t,b} = \frac{dr_f}{dt} - v_{g,b} = w - v_f \tag{19}$$

4 Model Evaluation

In the case of the fiber optic spark plugs, the measured flame growth rate w and the estimated flame burning velocity $S_{t,b}$ are the average rate of flame kernel velocity when the flame is 5 mm in radius, respectively. In order to compare the cycle-averaged flame burning velocity $S_{t,b}$ measured by the VisioFlame fiber optic at a fixed 5 mm probe radius with the model. The ensemble-averaged flame burning velocity $\langle S_{L,b}^c \rangle$ when $r_f = 5$ mm is calculated from the flame radius evolution predicted detailed in Sec. 2.

The ensemble-averaged laminar flame burning velocity $\langle S_{L,b}^c \rangle$ is calculated for each of the operating conditions with various spark timings and EGR rates. The ignition power of the arc and glow phase P_{ag} is assumed as 50 W for all the conditions. This approximate value is obtained from secondary ignition voltage and current measurements. The breakdown phase accounts for a small (less than 5%) percentage of ignition power and is neglected in the current work. During the arc and glow phase of spark ignition, only a fraction of the ignition energy is deposited into the gas due to heat loss to spark plug electrode and flow conditions [15]. The global efficiency of the arc and glow phase was estimated around 30% [10]. Thus, we introduce the ignition efficiency η_s, where the ignition power released to gas is estimated as

$$P_s = \eta_s \times P_{ag} = 0.3 \times 50 = 15\,\text{W} \tag{20}$$

The normalization following Eq. (2) is the single input to the flame kernel model and is shown in Fig. 9.

The modeled ensemble average flame burning velocity $\langle S_{L,b}^c \rangle$ is shown as crosses in Fig. 10. The cycle-averaged flame burning velocity $S_{t,b} = w - v_f$ measured from the VisioFlame fiber optic spark plugs is shown as circles with the margin of uncertainty quantified with the error bar defined by the standard deviation $\pm \sigma$ of $S_{t,b}$ over 2000 cycles. Both the modeled ensemble average laminar flame burning velocity $\langle S_{L,b}^c \rangle$ and the VisioFlame measured cycle-averaged flame burning velocity $S_{t,b} = w - v_f$ decrease with higher EGR rates and more advanced spark timing with lower temperature caused by the recirculated gas and early compression, respectively. The cycle-averaged flame burning velocity $S_{t,b}$ is more sensitive to the change in spark timing possibly due to the compression-induced in-cylinder flow condition.

Figure 11 further illustrates the accuracy of the modeled ensemble-averaged laminar flame burning velocity $\langle S_{L,b}^c \rangle$, which
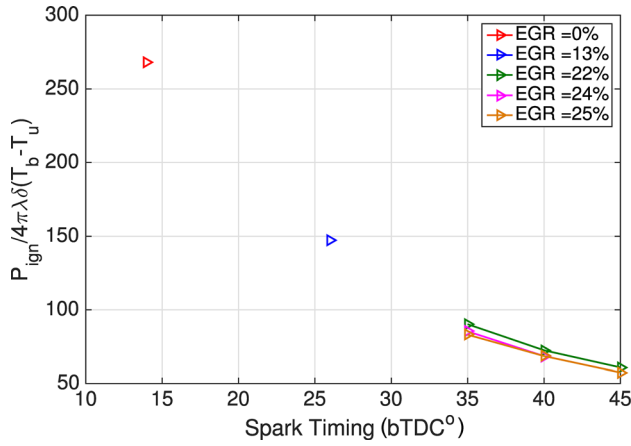
Fig. 9 Normalized ignition power $\widetilde{P}_s = P_s/(4\pi\lambda\delta^0(T_b - T_u))$
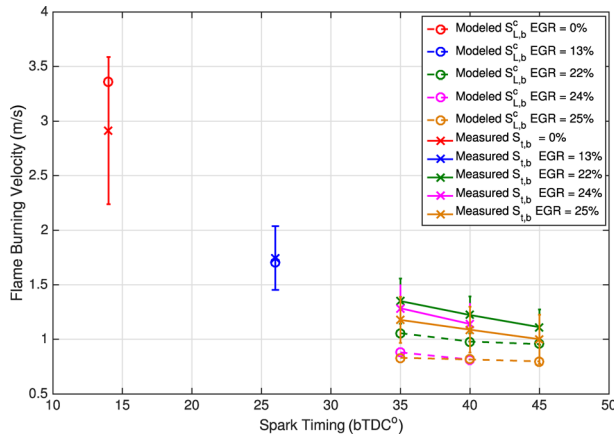

Fig. 10 Measured flame burning velocity $S_{t,b}$ (in circles) and modeled flame burning velocity $\langle S_{L,b}^c \rangle$ (in crosses)
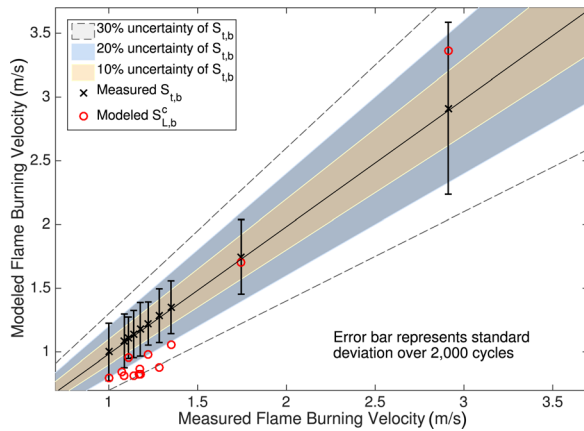

Fig. 11 Accuracy of the modeled flame burning velocity

is plotted as scatter dots against measured cycle-averaged flame burning velocity $S_{t,b} = w - v_f$. The 5%, 10%, and 20% variations from the mean are shown as shaded area, where the error bar represents the standard deviation of $S_{t,b}$ over 2000 cycles. It is shown that the model consistently underestimates flame speeds at higher EGR rate. This may be caused by neglecting the turbulent flame stretch during the initial growth of the flame kernel to a size of 5 mm radius. Thus, without considering the effect of in-cylinder flow, the modeled ensemble average laminar flame burning

velocity $\langle S_{L,b}^c \rangle$ agrees with the VisioFlame measured cycle-averaged flame burning velocity $S_{t,b}$ within 30% uncertainty. This is considered to be a reasonable margin of uncertainty since 20% uncertainty equals $\pm$ one standard deviation over 2000 cycles.

5 Conclusion

A flame curvature correction method is used to account for both the effect of flame stretch and deposition of ignition energy in a variable volume engine system. A physics-based model of cycle-averaged flame burning velocity has been developed and validated with flame velocity measurements from AVL VisioFlame fiber optic spark plug at operating conditions with various EGR rate and spark timing at misfire limits.

The laminar burning velocity predicted by the model are compared with flame burning velocities obtained experimentally with fiber optic spark plug measurements. The modeled laminar flame burning velocity matches the measured cycle-averaged flame burning velocity dependence on EGR rate, while the measured flame burning velocity is more sensitive to spark timing. However, without correction of the in-cylinder turbulent enhancement, the modeled laminar flame burning velocity is within 30% uncertainty. This is considered to be a reasonable margin of uncertainty since 20% uncertainty equals $\pm$ one standard deviation over 2000 cycles. Considering the turbulent effect and careful tuning of parameters, i.e., $\theta_{IV\,C}$ could achieve better matching with the data.

The methodology can also be extended to predict the misfire occurrence and the combustion cyclic variability by introducing cyclic variations in ignition power, thermodynamic states, and mixture properties.

Acknowledgment

Nomenclature

c_p = constant pressure specific heat
CAD = crank angle degree
CFD = computational fluid dynamics
D = mass diffusivity of the fuel
$\widetilde{e}_T$ = expansion ratio
IVC = intake valve closing
K = curvature stretch rate
Le = Lewis number
MBT = maximum break torque
P = in-cylinder pressure
P_{ag} = ignition power during arc and glow phase
P_{im} = intake manifold pressure
P_s = ignition power
$\widetilde{P}_s$ = normalized nondimensional ignition power
PFI = port fuel injection
q = energy flux over flame front area
r = modeled flame radius
$\widetilde{\mathbf{R}}$ = normalized flame radius trajectory
r_f = equivalent flame radius in experimental measurement
$\mathbf{R}_f$ = trajectory of flame ball radius at a given crank angle
$S_{t,b}$ = measured flame burning velocity
$S_{L,u}^0$ = laminar burning velocity with respect to the unburned gas
$S_{L,b}^0$ = laminar burning velocity with respect to the burned gas
$S_{L,b}^c$ = laminar burning velocity with respect to the burned gas corrected for curvature

$\langle S_{L,b}^c \rangle$ = ensemble-averaged laminar flame burning velocity
SI = spark-ignited
t = flame ball time trajectory at given crank angle
$\widetilde{t}$ = normalized nondimensional flame time
t_θ = time since ignition
T_b = adiabatic flame temperature
T_{egr} = EGR runner temperature
T_{exh} = exhaust runner temperature
$\widetilde{T}_f$ = normalized flame front temperature
T_{im} = intake manifold temperature
T_u = unburned gas temperature
t_f^0 = reaction front time scale
$\widetilde{\mathbf{U}}$ = normalized flame speed trajectory
V = volume
v_f = measured flame drift velocity
$v_{g,b}$ = burned gas velocity
$v_{g,u}$ = unburned gas velocity
w = measured flame growth rate
x_{egr} = external EGR mass fraction
x_{ir} = internal EGR mass fraction
x_r = total residual mass fraction
Z = Zel'dovich number
γ = polytropic exponent
δ^0 = laminar flame thickness
η_s = ignition efficiency
θ = crank angle
θ_s = ignition timing
λ = thermal conductivity
ρ_b = burned gas density
ρ_u = unburned gas density
σ = standard deviation
Φ = equivalence ratio
ϕ' = fuel to charge equivalence ratio

Appendix: Derivation of the Flame Kernel Initiation Model

Assume a constant volume system, the energy equation is written below accounting for changes in the system specific internal energy due to boundary work, heat conduction, heat release via combustion, and advective energy flows across the control surface of a differential control volume

$$\rho \frac{\partial h}{\partial t} - \frac{\partial P}{\partial t} = -\nabla \cdot \mathbf{q_x} + q_{ch} \tag{A1}$$

where the ignition energy term is represented by the spatial energy flux q_x integrated over flame front area.

According to Fourier law, the thermal heat conduction through a medium is

$$\mathbf{q_x} = -\lambda \nabla T \tag{A2}$$

With uniform pressure, $\partial P/\partial t$ is neglected, and the energy conservation term can be expressed as

$$\rho c_p \frac{\partial T}{\partial t} - \nabla \cdot \lambda \nabla T - q_{ch} = 0 \tag{A3}$$

with the Laplacian operator in Cartesian and spherical coordinate system as

$$\nabla^2 \cdot T = \frac{\partial^2 T}{\partial x^2} + \frac{\partial^2 T}{\partial y^2} + \frac{\partial^2 T}{\partial z^2}$$
$$= \frac{1}{r^2} \frac{\partial}{\partial r}\left(r^2 \frac{\partial T}{\partial r}\right) + \frac{1}{r^2 \sin\theta} \frac{\partial}{\partial \theta}\left(\sin\theta \frac{\partial T}{\partial \theta}\right) + \frac{1}{r^2 \sin^2\theta} \frac{\partial^2 T}{\partial^2 \phi} \tag{A4}$$

Assuming a homogeneous symmetric spherical system, the energy conservation equation is simplified as

$$\rho c_p \frac{\partial T}{\partial t} = \frac{1}{r^2} \frac{\partial}{\partial r}\left(r^2 \lambda \frac{\partial T}{\partial r}\right) + q_{ch} \tag{A5}$$

With a similar approach to the one described above, energy and species conservation can be expressed as follows:

$$\rho C_p \frac{\partial T}{\partial t} = \frac{1}{r^2} \frac{\partial}{\partial r}\left(r^2 \lambda \frac{\partial T}{\partial r}\right) + q\omega \tag{A6a}$$

$$\rho \frac{\partial Y}{\partial t} = \frac{1}{r^2} \frac{\partial}{\partial r}\left(r^2 \rho D \frac{\partial Y}{\partial r}\right) - \omega \tag{A6b}$$

The radius, time, temperature, and fuel mass fraction can be normalized as

$$\widetilde{r} = \frac{r}{\delta_f^0}, \quad \widetilde{t} = \frac{t}{\delta_f^0/S_L^0}, \quad \widetilde{T} = \frac{T - T_\infty}{T_{ad} - T_\infty}, \quad \widetilde{Y} = \frac{Y}{Y_\infty} \tag{A7}$$

The chemical reaction rate can be normalized as

$$\widetilde{\omega} = \frac{\omega \delta_f^0}{\rho S_L^0 Y_\infty} \tag{A8}$$

The nondimensional equations of Eq. (A6) can be expressed as

$$\frac{\partial \widetilde{T}}{\partial \widetilde{t}} = \frac{1}{\widetilde{r}^2} \frac{\partial}{\partial \widetilde{r}}\left(\widetilde{r}^2 \frac{\partial \widetilde{T}}{\partial \widetilde{r}}\right) + \widetilde{\omega} \tag{A9a}$$

$$\frac{\partial \widetilde{Y}}{\partial \widetilde{t}} = \frac{\mathrm{Le}^{-1}}{\widetilde{r}^2} \frac{\partial}{\partial \widetilde{r}}\left(\widetilde{r}^2 \frac{\partial \widetilde{Y}}{\partial \widetilde{r}}\right) - \widetilde{\omega} \tag{A9b}$$

where the Lewis number is given as $\mathrm{Le} = \lambda/\rho c_p D$.

Currently, all the above equations follow the Eulerian specifications. Attaching the coordinate to the moving flame front $R = R(t)$, the Eulerian specifications is transformed to the Lagrangian specifications. So the nondimensional equations can be rewritten in Lagrangian specifications in Eq. (A10) with the flame front propagating speed $\widetilde{U}$ defined as $\widetilde{U}(t) = d\widetilde{R}(t)/d\widetilde{t}$

$$\frac{\partial \widetilde{T}}{\partial \widetilde{t}} - \widetilde{U} \frac{\partial \widetilde{T}}{\partial \widetilde{r}} = \frac{1}{\widetilde{r}^2} \frac{\partial}{\partial \widetilde{r}}\left(\widetilde{r}^2 \frac{\partial \widetilde{T}}{\partial \widetilde{r}}\right) + \widetilde{\omega} \tag{A10a}$$

$$\frac{\partial \widetilde{Y}}{\partial \widetilde{t}} - \widetilde{U} \frac{\partial \widetilde{Y}}{\partial \widetilde{r}} = \frac{\mathrm{Le}^{-1}}{\widetilde{r}^2} \frac{\partial}{\partial \widetilde{r}}\left(\widetilde{r}^2 \frac{\partial \widetilde{Y}}{\partial \widetilde{r}}\right) - \widetilde{\omega} \tag{A10b}$$

Assuming a quasi-steady-state flame front $\partial/\partial \widetilde{t} = 0$, the nondimensional equations in Eq. (A10) are simplified as

$$-\widetilde{U} \frac{d\widetilde{T}}{d\widetilde{r}} = \frac{1}{\widetilde{r}^2} \frac{d}{d\widetilde{r}}\left(\widetilde{r}^2 \frac{d\widetilde{T}}{d\widetilde{r}}\right) + \widetilde{\omega} \tag{A11a}$$

$$-\widetilde{U} \frac{d\widetilde{Y}}{d\widetilde{r}} = \frac{\mathrm{Le}^{-1}}{\widetilde{r}^2} \frac{d}{d\widetilde{r}}\left(\widetilde{r}^2 \frac{d\widetilde{Y}}{d\widetilde{r}}\right) - \widetilde{\omega} \tag{A11b}$$

Derivations from the energy equations that yields the theoretical relationship between the nondimensional normalized flame radius $\widetilde{R} = R_f/\delta^0$ and flame burning velocity $\widetilde{U} = S_{L,b}/S_{L,b}^0$ are detailed in Chen and Ju [5].

The assumption of negligible $\partial P/\partial t$ in Eq. (A3) likely has a secondary effect on burning velocity. As shown in Fig. 6, for the first 20 crank angle degrees after the start of ignition, there is a large rate of decrease in the corrected flame burning speed S_{lb}^c compared with the unstretched flame burning velocity S_{lb}^0. This indicates that the flame speed is varying mainly as a result of curvature-based stretch $(2/RdR/dt)$, which is offset in part by the ignition energy deposition. The change in pressure and unburned

temperature have a less significant effect on burning velocity, considering the minor changes in S_{lb}^0. In future work, the errors associated with neglecting the $\partial P/\partial t$ term can be evaluated with detailed flame simulations considering this effect.

References

[1] Aleiferis, P. G., Taylor, A. M. K. P., Whitelaw, J. H., Ishii, K., and Urata, Y., 2000, "Cyclic Variations of Initial Flame Kernel Growth in a Honda VTEC-E Lean-Burn Spark-Ignition Engine," SAE Paper No. 2000-01-1207.

[2] Sun, Z., and Zhu, G. G., 2015, *Design and Control of Automotive Propulsion Systems*, 1st ed., CRC Press Taylor Francis Group, Boca Raton, FL.

[3] Quader, A., 1976, "What Limits Lean Operation in Spark Ignition Engines–Flame Initiation or Propagation?" SAE Paper No. 760760.

[4] Bianco, Y., Cheng, W.-K., and Heywood, J. B., 1991, "The Effects of Initial Flame Kernel Conditions on Flame Development in SI Engine," SAE Paper No. 912402.

[5] Chen, Z., and Ju, Y., 2007, "Theoretical Analysis of the Evolution From Ignition Kernel to Flame Ball and Planar Flame," Combust. Theory Modell., **11**(3), pp. 427–453.

[6] Middleton, R. J., Martz, J. B., Lavoie, G. A., Babajimopoulos, A., and Assanis, D. N., 2012, "A Computational Study and Correlation of Premixed Isooctane Air Laminar Reaction Fronts Diluted With EGR," Combust. Flame, **159**(10), pp. 3146–3157.

[7] Ronney, P. D., and Sivashinsky, G. I., 1989, "A Theoretical Study of Propagation and Extinction of Nonsteady Spherical Flame Fronts," SIAM J. Appl. Math., **49**(4), pp. 1029–1046.

[8] Naziev, Y. M., Aliev, M. A., and Efendiev, V. S., 1974, "Thermophysical Properties of A-72 Gasoline at Various Temperatures and Pressures," Pet. Gas Process. Chem. Technol. Fuels Oils, **10**(8), pp. 626–628.

[9] Peters, N., 2000, *Turbulent Combustion*, 1st ed., Cambridge University Press, Cambridge, UK.

[10] Heywood, J., 1988, *Internal Combustion Engine Fundamentals*, 1st ed., McGraw-Hill Science/Engineering/Math, New York.

[11] Eriksson, L., and Andersson, I., 2002, "An Analytic Model for Cylinder Pressure in a Four Stroke SI Engine," SAE Paper No. 2002-01-0371.

[12] Chung, S., and Law, C., 1988, "An Integral Analysis of the Structure and Propagation of Stretched Premixed Flames," Combust. Flame, **72**(3), pp. 325–336.

[13] AVL, 2004, "AVL VisioFlame Kernel Application Software," Software Version 1.1 and Later ed., AVL List GmbH, Graz, Austria.

[14] Andrews, G. E., and Bradley, D., 1972, "Determination of Burning Velocities: A Critical Review," Combust. Flame, **18**(1), pp. 133–153.

[15] Richard, S., Dulbecco, A., Angelberger, C., and Truffin, K., 2015, "Development of a One-Dimensional Computational Fluid Dynamics Modeling Approach to Predict Cycle to Cycle Variability in Spark Ignition Engines Based on Physical Understanding Acquired From Large Eddy Simulation," Int. J. Engine Res., **16**(3), pp. 379–402.